



PERGAMON

Available online at www.sciencedirect.com

SCIENCE @ DIRECT®

Engineering Fracture Mechanics 70 (2003) 2527–2542

Engineering
Fracture
Mechanics

www.elsevier.com/locate/engfracmech

Three-dimensional stress and deformation fields around flat and slant cracks under remote Mode I loading conditions

Elmoiz Mahgoub, Xiaomin Deng ^{*}, Michael A. Sutton

Department of Mechanical Engineering, University of South Carolina, Columbia, SC 29208, USA

Received 1 July 2002; received in revised form 24 December 2002; accepted 21 January 2003

Abstract

This paper investigates the phenomenon of slant fracture observed in stable tearing tests of many ductile materials, where an initially flat crack, loaded under remote Mode I conditions, tends to grow into a slant crack and stay in the slant configuration until final fracture. In an effort to identify potential reasons why cracks prefer to grow in a slant manner, three-dimensional finite element analyses of crack-front stress and deformation fields in Arcan-type specimens containing a flat or slant crack are performed under elastic–plastic and remote Mode-I loading conditions. In particular, the crack-tip opening displacement (COD) at a position behind the crack tip, the mean stress, the effective stress, and a constraint factor (defined as the ratio of the mean stress and effective stress) are studied and compared for the two types of cracks. Analysis results reveal several stress/deformation field variations around flat and slant cracks under identical remote loading conditions. First, close to the crack front, the COD of a slant crack is greater than that of a flat crack. Second, at the specimen's mid-plane, a flat crack leads to a higher constraint value ahead of the crack than a slant crack. Third, the effective stress ahead of a slant crack is greater than that ahead of a flat crack, especially close to the crack front. The above results seem to suggest that slant fracture may be preferred because a slant crack enhances the driving force in the form of a higher near-tip COD value and because a shearing type of failure is promoted in the case of a slant crack compared to a tensile type of failure in the case of a flat crack.

© 2003 Elsevier Ltd. All rights reserved.

Keywords: Slant crack; Slant fracture; Stable tearing; Constraint

1. Introduction

For thin sheets of many ductile materials, mixed-mode I/III fracture is considered a common failure mode [1–11]. In particular, this failure mode can take the form of slant fracture [1,2], which refers to the situation in which, for example, an initially flat crack in a sheet loaded in Mode I often tends to turn and grow along a slant plane. This situation is illustrated in Fig. 1, where both a typical fracture surface and a FE mesh [12] for the transition region are shown. Relevant studies in this area are discussed below, since they serve as the basis for the current investigation.

^{*} Corresponding author. Tel.: +1-803-777-7144; fax: +1-803-777-0106.

E-mail address: deng@enr.sc.edu (X. Deng).

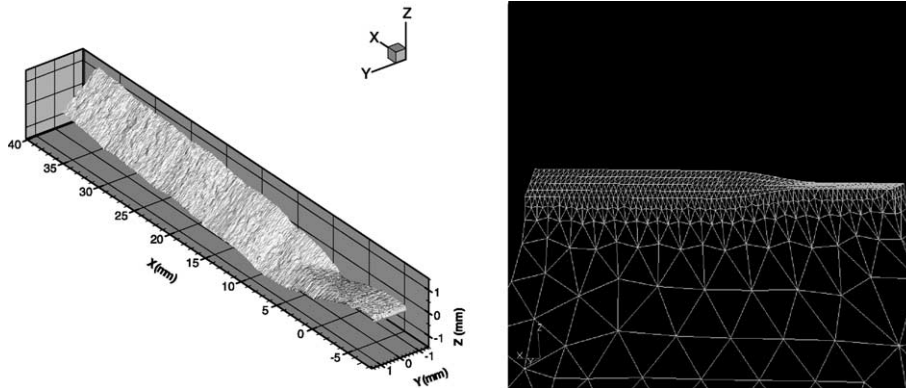


Fig. 1. Typical surface crack shape in Al 2024-T3 during slant crack transition and a finite element representation [12] of transition in an Arcan test specimen.

Dawicke and Sutton [13,14] studied the stable tearing behavior of middle-crack-tension or M(T) specimens made of aluminum alloy 2024-T3. They tested sheet specimens having initial flat cracks and slant cracks with a slant angle of 45° . Here the slant angle is defined as the angle between the slant plane (slant crack surface) and the flat crack surface (which intersects the lateral surfaces of the sheet with a right angle). They found that flat cracks under Mode I loading conditions underwent a transition to slant crack growth and that the critical crack-tip opening angle (CTOA) value measured on the specimen surface was lower in the case of a slant crack than in the case of a flat crack. To this end, it is noted that mixed-mode I/III fracture toughness tests [15] conducted on a range of materials, including steels and aluminum alloys, seem to show that ductile materials have reduced fracture toughness values for slant cracks.

Fracture surface analyses of M(T) stable tearing specimens made of Al 2024-T3 have been performed by Lloyd and Piascik [16]. Surface reconstruction results from microtopography data revealed that M(T) specimens in the L–T orientation (i.e., the load was applied in the longitudinal or rolling direction and the crack was in the transverse direction) exhibit a high degree of slant fracture. Shear lips were found to form along both sides of the specimen and grow to large sizes during stable tearing testing. Experimental studies by Amstutz et al. [17] and Boone [18] showed that an initially flat crack in an Al 2024-T3 specimen loaded in tension would grow into a slant crack, with a slant angle of about 38° for most of the remaining fracture process.

The reason why slant fracture occurs and why a crack loaded in Mode I tends to grow in an almost constant slant plane is still not well understood. It is clear, however, that slant fracture changes a Mode-I type of crack growth to a mixed-mode I/III type of crack growth. It seems that mixed-mode I/III fracture may have a reduced fracture toughness value when compared to Mode I fracture (e.g. [1,2,5,10]), but the mechanics underlying slant fracture is still not clear.

It is the purpose of the current study to try and shed some light on the slant fracture process and its underlying mechanics. To this end, detailed three-dimensional (3D) finite element analyses have been carried out in order to understand crack-front stress and deformation fields around flat and slant cracks under identical static but nominally Mode I loading conditions. By analyzing the differences in the crack-front stress and deformation fields around the two types of cracks, it is hoped that mechanics insights can be gained about the slant fracture transition phenomenon. The problem geometry and material are those of a modified Arcan specimen [17]. The general-purpose finite element code ANSYS [19] is used for the numerical studies.

1723.8 MPa (250 ksi). Due to the thickness and high yield stress, the stainless steel fixture remained elastic throughout the experiment. In the specimen region, the aluminum alloy has a Young's modulus, E , of 71.71 GPa (10.35E6 psi), a Poisson's ratio, ν , of 0.3, and an initial yield stress, σ_0 of 358.5 MPa (52 ksi). The flow stress vs. plastic strain for Al 2024-T3 during uniaxial loading is presented in Fig. 3 to quantify the strain hardening behavior. In the finite element simulation both materials are modeled with an isotropic strain hardening behavior.

The Arcan specimen is loaded in Mode I, namely with $\phi = 0^\circ$ in Fig. 2(a), so that the fixture grip holes at the two ends of the centerline are gradually pulled away from each other. The maximum displacement loading applied between the grip holes corresponds to the measured value just before initial crack growth in the actual stable tearing test. The corresponding mode I stress intensity factor $K_I \sim 33.2 \text{ MPa} \sqrt{\text{m}}$.

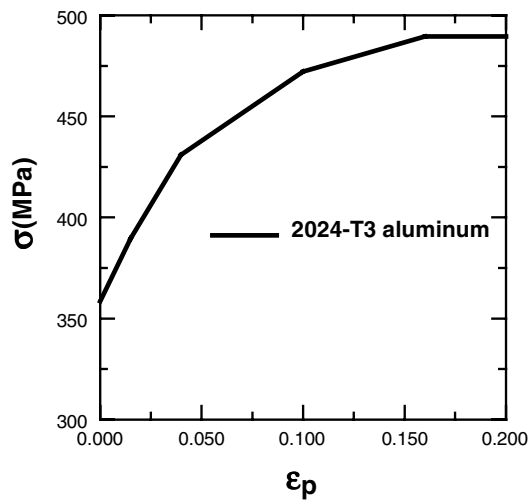


Fig. 3. Strain hardening curve for aluminum alloy 2024-T3.

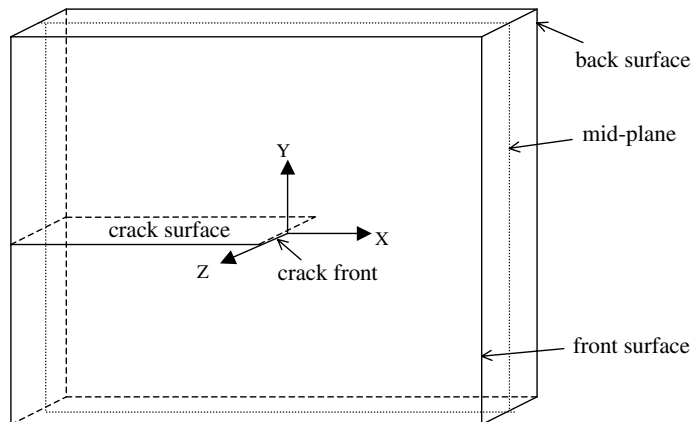


Fig. 4. A single-edge crack specimen with a flat crack, where X , Y , Z serve both as the global coordinate system and the crack-front local coordinate system.

2.1. Finite element mesh in the case of a flat crack

Before discussing the mesh design, a schematic is presented in Fig. 4 to illustrate a single-edge crack specimen with a flat crack. The front and back surfaces of the sheet specimen as well as its mid-plane are defined in the figure. A global coordinate system is also shown in the figure, with the origin placed at the midpoint of the straight crack front (which is normal to the front and back surfaces). The X axis lies in the crack surface plane and is perpendicular to the crack front; the Y axis is normal to the crack surface plane; and the Z axis is along the crack front, forming a right-hand system with the X and Y axes. The above so defined coordinate system also serves as a convenient crack-front local coordinate system.

Only half of the geometry in the thickness direction needs to be modeled due to symmetry about the mid-plane, which is located at $Z = 0$. A converged 3D finite element mesh is shown in Fig. 5, where one-half of the specimen is meshed with 10 layers of elements in the thickness direction and one-half of the fixture region with 16 layers, six layers extending beyond the specimen thickness. The layer interfaces are located at

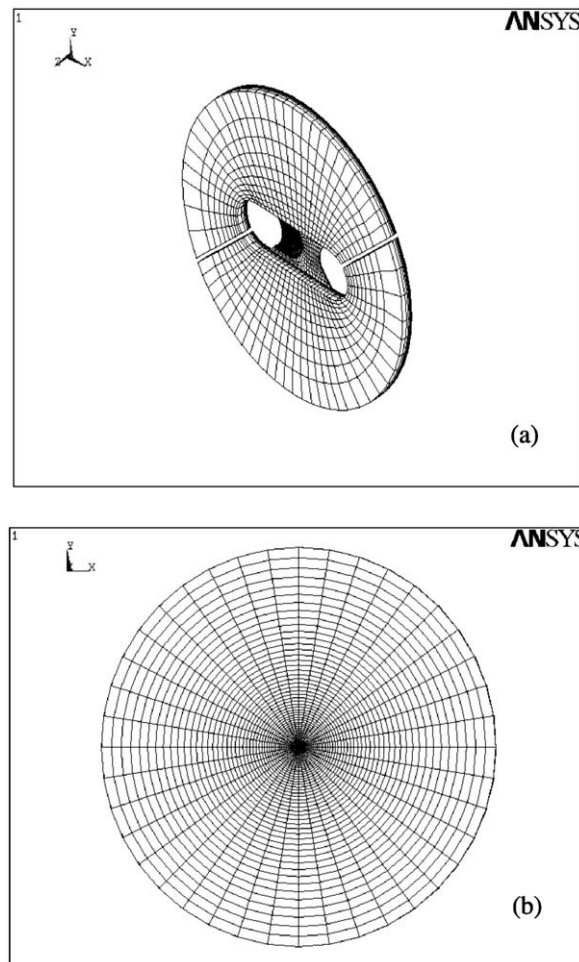


Fig. 5. A converged finite element mesh in the case of a flat crack, representing one half of the Arcan fixture–specimen system in the thickness direction: (a) an overall view; (b) an X – Y plane view around the crack front (the center point), where the flat crack lies to the left of the center point.

distances of $Z = 0.2635, 0.4727, 0.6387, 0.7704, 0.875, 0.958, 1.024, 1.076, 1.118, \text{ and } 1.15$ mm. The total mesh consists of 37,260 eight-node brick elements (of which 27,660 are in the specimen region and 9600 in the fixture region) with a total of 42,504 nodes. A focused circular mesh with 50 rings in the X – Y plane (see Fig. 5(b)) is employed near the crack front to capture detailed stress/strain variations and their singularity behavior at the crack front. Smaller elements, with edge sizes on the order of 0.0218 mm (0.00086 in.), are distributed along the first ring around the crack front. Elements with larger edge sizes are used in rings further away from the crack front.

The connection between the fixture and specimen is idealized by a rigid and continuous joint, as suggested by Deng and Newman [22] based on the fact that the fixture and pins used in Arcan tests are relatively rigid compared to the specimen. Thus in the finite element analysis, the specimen–fixture system is treated as one continuous solid with two regions of different thickness and material properties. Also due to the fixture rigidity, the effect of omitting the loading holes on the load transfer to the specimen is expected to be insignificant [22].

Loading of the specimen is achieved by specifying a maximum displacement value in the Y -direction ($U_y = 0.116$ mm) at the set of upper-loading nodes, which are defined as the nodes along the through-thickness line that represents the upper Mode-I loading hole (relative to the fixture/specimen orientation in Fig. 5). The corresponding nodes at the bottom are fixed in all directions ($U_x = U_y = U_z = 0$). The symmetry about the mid-plane requires that all nodes lying on that plane must be fixed in the z -direction ($U_z = 0$). To remove rigid body rotation about the Z -axis, a zero U_x displacement value can be specified at any one node. For convenience, the mid-plane node at the location of the upper Mode-I loading hole is chosen for that purpose.

2.2. Finite element mesh in the case of a slant crack

A schematic of a single-edge crack specimen with a slant crack is shown in Fig. 6, where the slant crack surface plane is at an angle (the slant angle α) with that of a flat crack. The global coordinate system (X, Y, Z) is as defined in Fig. 4 for a flat crack. For discussion of stress and deformation fields around the straight crack front, a local coordinate system (x, y, z) is also defined, where x coincides with X , y is perpendicular to the slant crack surface, and z is along the straight crack front direction. The experimentally measured slant angle from [17] (which is 38°) is used in this study.

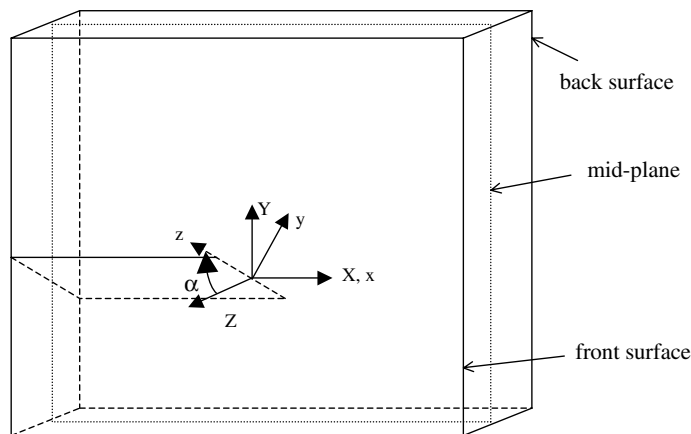


Fig. 6. A single-edge crack specimen with a slant crack, where X, Y, Z serve as the global coordinate system while x, y, z as the crack-front local coordinate system.

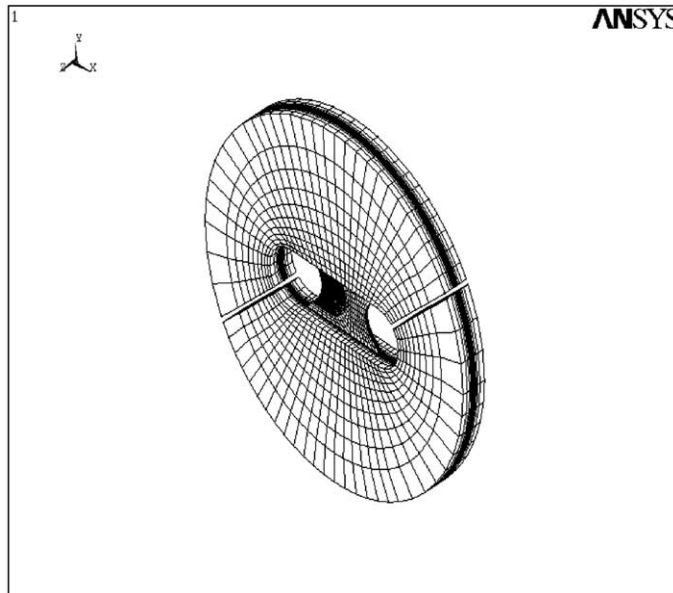


Fig. 7. A converged finite element mesh in the case of a slant crack, for the Arcan fixture–specimen system.

The entire fixture–specimen system is modeled in the case of a slant crack due to the lack of any symmetry. Shown in Fig. 7 is a converged finite element mesh for the slant crack case. The specimen region is meshed with 20 layers in the thickness direction. Since the fixture is thicker than the specimen, it is meshed with six additional layers beyond the specimen thickness on either side of the specimen surfaces. The spacing of the specimen layer interfaces is similar to those given for the flat crack, with the complete mesh being composed of 74,520 eight-node brick elements (of which 55,320 are in the specimen region and 19,200 in the fixture region) with a total of 81,516 nodes. Displacement loading conditions identical to those used in the case of a flat crack are applied.

3. Results and discussion

3.1. COD variation

In this study, a COD vector, which is a function of distance to the crack front, is defined in the local coordinate system as $\mathbf{v} = \delta_x \mathbf{e}_x + \delta_y \mathbf{e}_y + \delta_z \mathbf{e}_z$, where \mathbf{e}_x , \mathbf{e}_y and \mathbf{e}_z are, respectively, the base vectors along the local x , y and z -directions, and δ_x , δ_y and δ_z are, respectively, the local shearing (Mode II), opening (Mode I) and tearing (Mode III) components of the COD vector. The basis for a COD criterion in fracture predictions has been discussed extensively [21,23], and experimental evidence for use of a mixed mode COD criterion presented (e.g., [17,18,24]). Based on this work, the individual COD components are defined as follows:

$$\delta_x = U_x^+ - U_x^-; \quad \delta_y = U_y^+ - U_y^-; \quad \delta_z = U_z^+ - U_z^- \quad (1)$$

where U_x^+ , U_y^+ and U_z^+ are, respectively, local x , y and z displacement components of the upper crack surface (on the side with positive y), while U_x^- , U_y^- and U_z^- are, respectively, the corresponding displacement components of the lower crack surface. The magnitude of the COD vector is referred to as the total COD or

δ_t , where $\delta_t = |\text{COD}| = (\delta_x^2 + \delta_y^2 + \delta_z^2)^{1/2}$. Note that a Mode-I CTOA value (e.g. [13,14]) can be converted to an equivalent Mode-I COD value near the crack tip when the crack opening angle is approximately constant in the crack tip region.

Variations of the total COD and local COD components with distance from the crack front are shown in Figs. 8–10 for the slant crack specimen. In particular, Fig. 8 shows the variations at the specimen’s mid-plane, Fig. 9 the variations at the specimen’s front surface, and Fig. 10 at the back surface. Based on the data in these figures, the following observations can be made. First, near the crack front (see Figs. 8(a), 9(a), 10(a)), the local tearing component δ_z is the largest COD component, with its value close to that of δ_t . Second, the local opening component δ_y is smaller than the local tearing component near the crack front

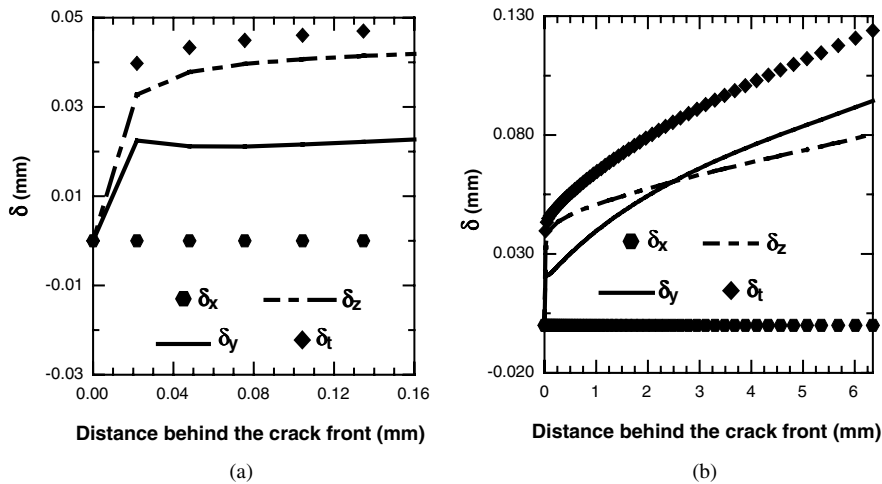


Fig. 8. Variations of the total COD and local COD components at the mid-plane of the slant crack specimen: (a) a crack-front local view; (b) an overall view.

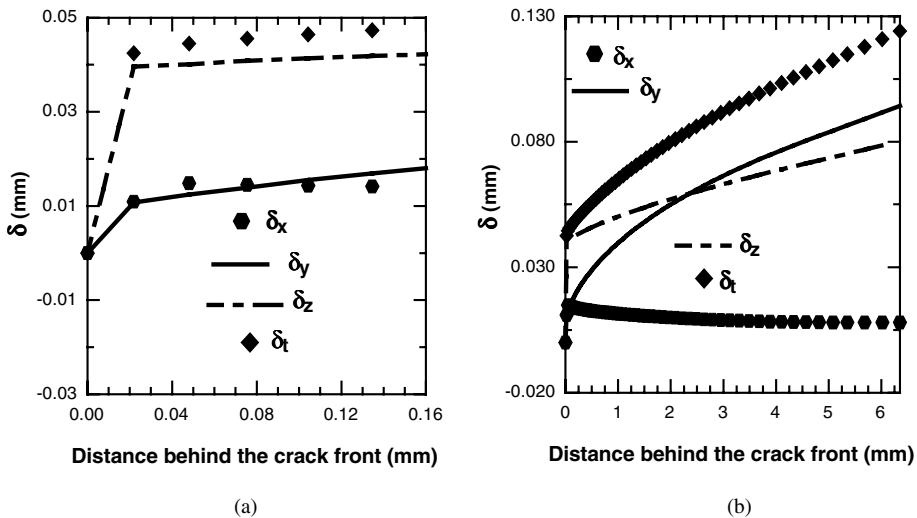


Fig. 9. Variations of the total COD and local COD components at the front surface of the slant crack specimen: (a) a crack-front local view; (b) an overall view.

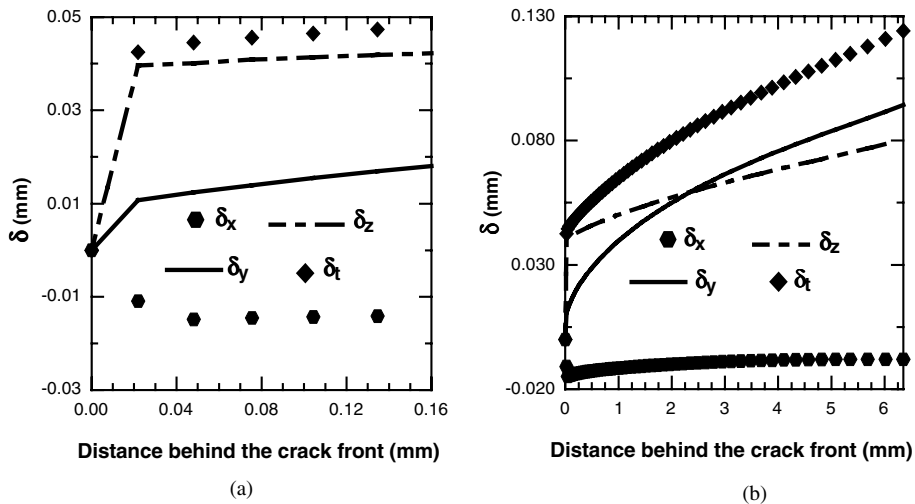


Fig. 10. Variations of the total COD and local COD components at the back surface of the slant crack specimen: (a) a crack-front local view; (b) an overall view.

but becomes the largest component further away from the crack front, with the transition at a distance of about 2.3 mm (which is the specimen thickness). It is noted that the tearing component is of the same order of magnitude as the opening component after the latter becomes the largest component; thus both components contribute, almost equally, to δ_r . The local shearing component, δ_x , has the expected value of zero at the mid-plane due to anti-symmetry. It has a nonzero but insignificant value at the front and back surfaces near the crack front (due to the asymmetry between the front and back surfaces) and becomes zero further away from the crack front.

An immediate, and somewhat obvious, conclusion from the above observations is that, the slant fracture process is controlled both by the crack-front separation, which may be represented by the local opening COD component, and by the crack-front tearing, which may be represented by the local tearing COD component. This is consistent with the view [7] that material damage ahead of the crack front occurs as a consequence of a local tearing or Mode III loading, while the local opening or Mode I loading simply acts to separate the extensively damaged specimen halves. It may be stated that, although a specimen with a slant crack is subjected to remote Mode I loading, a significant local tearing COD component suggests that a slant crack promotes local mixed-mode I/III loading conditions at the crack front.

To seek insight into possible reasons why a flat crack may prefer to grow into a slant crack, a comparison of the variations in δ_r behind the crack front is made between the flat and slant crack cases, as shown in Fig. 11. This figure includes the variations at the specimens' mid-plane as well as the front and back surfaces to provide some sense of changes in the thickness direction. While the overall view of the variation comparison (see Fig. 11(b)) indicates that there is little difference between the flat and slant crack solutions away from the crack-front region, the crack-front local view (see Fig. 11(a)) clearly shows that δ_r in the slant crack case is greater than that in the flat crack case at small distances behind the crack front. In light of this observation, it can be argued that, under the same remote loading, it will be easier for the slant crack, than the flat crack, to grow if we view the COD value near the crack front as the crack-growth driving force and if we assume that the fracture toughness in terms of a critical COD is the same in both flat and slant crack cases. To this end, it is noted that the results of a previous study [13] show that, during initial crack growth, flat cracks have a higher critical surface CTOA value than slant cracks do, which seems to enhance the probability of the preceding argument.

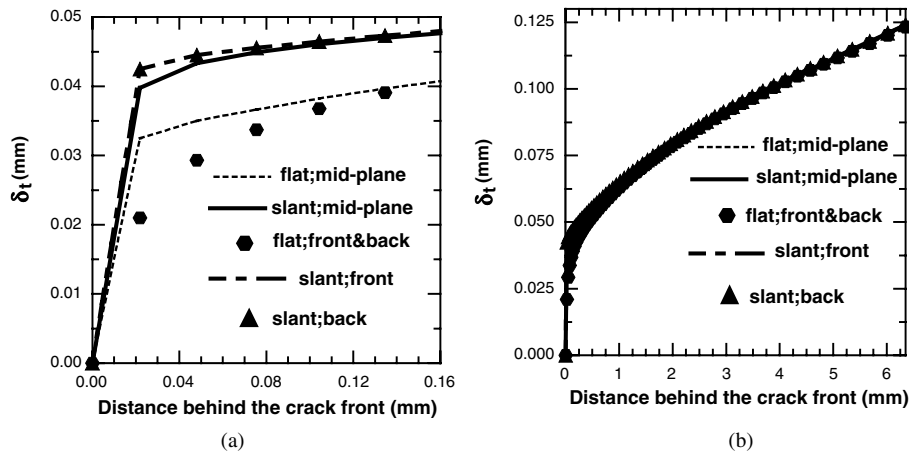


Fig. 11. A comparison of the total COD variation for the flat and slant crack cases: (a) a crack-front local view; (b) an overall view.

Another observation is that, while in the case of the flat crack the COD just behind the crack front is greater at the mid-plane than at the front and back surfaces, the COD in the case of the slant crack is almost the same at the mid-plane and at the front and back surfaces. Suppose again that the local COD can be viewed as the crack-growth driving force and that there exists a constant fracture toughness in terms of a critical COD value. The fact that the crack-growth driving force for the slant crack is the same at the mid-plane and at the front and back surfaces suggests that the crack front in the slant crack case will tend to advance uniformly, with no or only slight tunneling. For the flat crack, on the other hand, the fact that the local COD at the mid-plane is greater than that at the front and back surfaces implies that the flat crack will probably experience more crack tunneling than the slant crack. These statements are fully consistent with previous experimental observations [13,14,18].

3.2. Stress variations

The radial and angular variations of stress components in the crack-front local coordinate system are presented in this section. Solutions for the flat and slant crack cases are compared and implications are discussed.

For the flat crack specimen, the local and global coordinate systems are the same. In this case, stress variations at three through-thickness locations (the mid-plane and the front and back surfaces) are taken from planes parallel to the X - Y plane, and the radial and angular directions are those usually associated with a local polar coordinate system (r, θ) in a plane, with $r = 0$ at the crack front and $\theta = 0^\circ$ along the positive X direction.

For the slant crack specimen, the local and global coordinate systems are different. In this case, three planes at different thickness locations that are parallel to the local x - y plane are used to abstract the stress variations. In particular, one of the planes intersects the crack front at the mid-point and is conveniently called the “mid-plane” here because of the fact that its counterpart in the flat crack case also intersects the crack front at the mid-point. The other two planes intersect the crack front at the two end points on the front and back surfaces of the specimen and are also conveniently called, respectively, the “front” and “back” surfaces, mirroring the names of their counterparts in the flat crack case. Similar to the flat crack case, a local polar coordinate system (r, θ) can be associated with each of the three planes, with $r = 0$ at the crack front and $\theta = 0^\circ$ along the positive x direction (see Fig. 12).

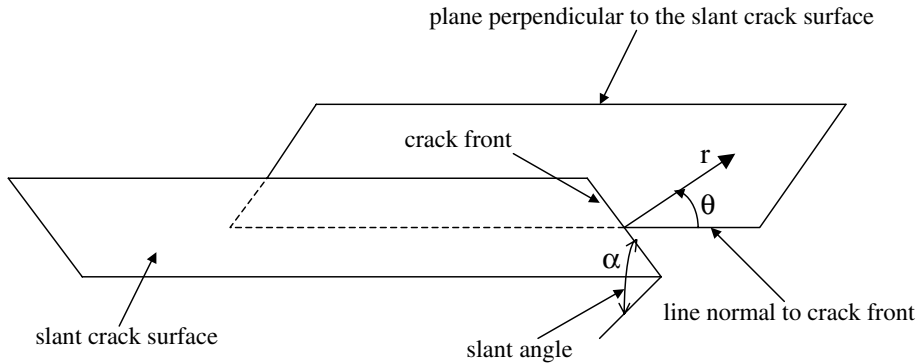


Fig. 12. A schematic definition of a local polar coordinate system that lies on a plane perpendicular to the surface of a slant crack and parallel to the local x - y plane (see Fig. 6), where r and θ are the polar coordinates.

3.2.1. Radial variations

The radial variation of the constraint factor, σ_m/σ_e , along the direction $\theta = 0^\circ$ is shown in Fig. 13, where σ_m is the mean stress and σ_e the effective stress. It is seen that, at the mid-plane, constraint rises quickly as the crack front is approached and it is greater in the flat crack case than in the slant crack case. In both cases, constraint near the crack front is much greater at the mid-plane than at the front and back surfaces. Further away from the crack front, constraint values at the mid-plane and at the front and back surfaces are insignificant and of the same order. Therefore, the main effect of a slant crack is that it significantly lowers the crack-front constraint value at the mid-plane relative to the flat crack case under identical remote loading conditions.

Fig. 14 describes the radial variations of the mean stress and effective stress along $\theta = 0^\circ$. The trend for the mean stress (Fig. 14(a)) is similar to that for the constraint factor, namely that the mean stress is small at the front and back surfaces and large at the mid-plane, and that the main effect of the slant crack

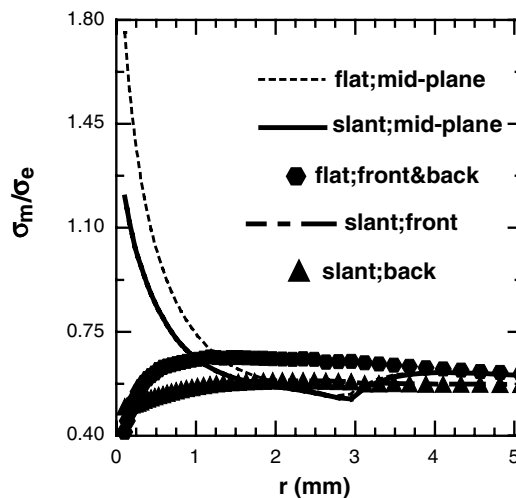


Fig. 13. Radial constraint variations along $\theta = 0^\circ$ at the mid-plane and front and back surfaces: a comparison of solutions for the flat and slant crack cases.

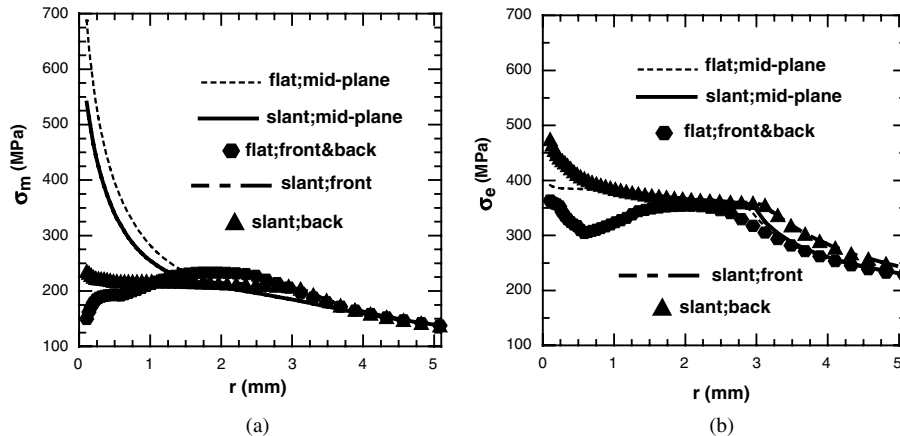


Fig. 14. Radial variations of (a) the mean stress and (b) the effective stress along $\theta = 0^\circ$ at the mid-plane and front and back surfaces: a comparison of solutions for the flat and slant crack cases.

configuration relative to the flat crack configuration is to reduce the crack-front level of the mean stress at the specimen's mid-plane.

Several observations can be made for the effective stress near the crack front (see Fig. 14(b)). First, in the flat crack case, σ_e is smaller at the front and back surfaces than at the mid-plane. Second, σ_e has lower values in the flat crack case than in the slant crack case. Third, in the slant crack case, σ_e has roughly the same values at the mid-plane and at the front and back surfaces (their values overlap each other). Thus, relative to the flat crack and under identical remote loading conditions, the slant crack is seen to be able to raise the level of the effective stress at both the specimen's mid-plane and at the specimen's front and back surfaces.

3.2.2. Angular variations

The radial variations in the preceding sections are along the direction directly ahead of the crack front and do not give an overall view of the stress quantities along other directions ahead of the crack. To this end, Figs. 15 and 16 provide angular variations of the stress quantities near the crack front for both the flat and slant crack cases, which will enable a better view and comparison of the stress fields. The angular variations are drawn along a circular path centered at the crack front, which is at a small radial distance of $r = 0.272$ mm away from the crack front (for comparison, the specimen thickness is 2.3 mm). The angular position in the figures is between 0° and 180° for the following reason. In the flat crack case, the angular variations of σ_m , σ_e and their ratio are symmetric with respect to $\theta = 0^\circ$, hence only the range ($0^\circ, 180^\circ$) is needed. The same is true at the mid-plane when a slant crack is concerned. At the "front" and "back" surfaces (which are not the actual front and back surfaces; see discussions in the first paragraph of Section 3.2 and Fig. 12) of a slant crack specimen, either the range ($0^\circ, 180^\circ$) or the range ($-180^\circ, 0^\circ$) is outside the specimen and only solutions for the remaining 180° -interval exist, which are presented in Figs. 15 and 16 using the absolute values of θ . It is noted that the slant crack solutions at the front crack surface and those at the back crack surface form anti-symmetric pairs about $\theta = 0^\circ$, which can be seen from the figures.

Angular constraint variations in the crack-front local coordinate system are shown in Fig. 15. In both flat and slant crack cases, the largest constraint is found to exist at the mid-plane, just ahead of the crack front. The constraint is almost constant at the mid-plane over the angular range of $0^\circ \leq \theta \leq 45^\circ$. The constraint in the rest of the domain is small. In the slant crack case, the constraint level at the front and back surfaces seems to decrease linearly and slowly with θ . Observations from Fig. 15 confirm the finding from the

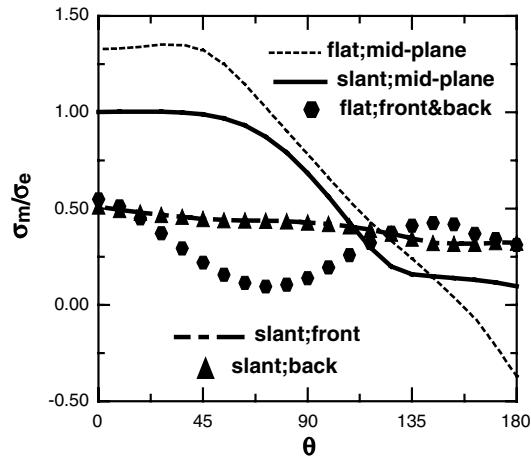


Fig. 15. Angular constraint variations along $r = 0.272$ mm at the mid-plane and front and back surfaces: a comparison of solutions for the flat and slant crack cases.

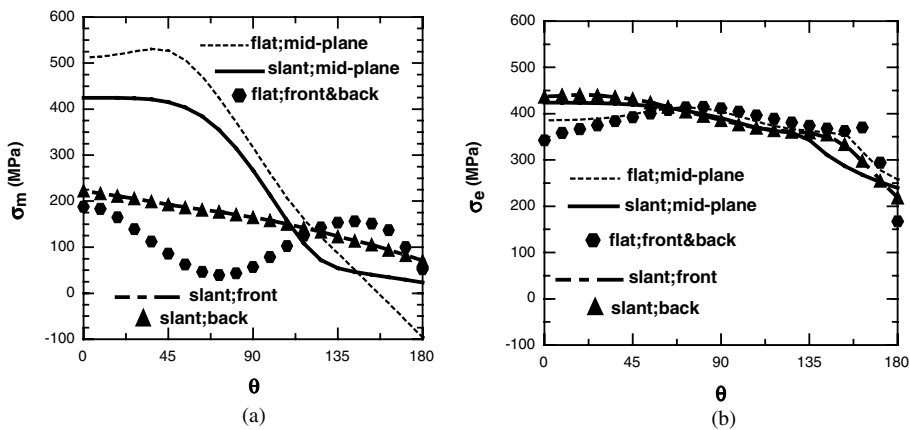


Fig. 16. Angular variations of (a) the mean stress and (b) the effective stress along $r = 0.272$ mm at the mid-plane and front and back surfaces: a comparison of solutions for the flat and slant crack cases.

previous section that a major effect of changing from a flat crack to a slant crack in a specimen is to lower the constraint level ahead of the crack front at the specimen's mid-plane.

The overall trend in the angular variation of the mean stress (Fig. 16(a)) is very similar to that of the constraint. Highest mean stress values occur at the mid-plane just ahead of the crack front, which are almost constant in the interval ($0^\circ, 45^\circ$), and these values are higher in the flat crack case than in the slant crack case. The mean stress variation in the slant crack case is almost linear at the front and back surfaces, with the maximum at $\theta = 0^\circ$.

Fig. 16(b) presents the angular variations of the effective stress. It is observed that the effective stress at the mid-plane and at the front and back surfaces is, over the range $0^\circ \leq \theta \leq 45^\circ$, greater in the slant crack case than in the flat crack case, with the maximum difference at $\theta = 0^\circ$. As seen earlier from comparisons of radial variations of the effective stress (see Fig. 14(b)), the values of this stress quantity at the mid-plane and

at the front and back surfaces just ahead of the crack front are basically the same in the slant crack case, while they are higher at the mid-plane and lower at the front and back surfaces in the flat crack case. Thus the effective stress at the front and back surfaces receive the largest elevation when a flat crack is changed to a slant crack.

A synopsis of observations from comparisons of stress variations in this and the preceding section is as follows. Under identical remote loading conditions, the crack front constraint and mean stress is lowered at the mid-plane and the effective stress is raised at both the mid-plane and at the front and back surfaces, when a through-thickness flat crack is replaced with a slant crack of the same length. Since high constraint and high mean stress are associated with tensile types of failure and high effective stress is indicative of shearing types of failure, the above observations suggest that a slant crack tends to suppress tensile failure and enhance shearing failure. Furthermore, the above observations may be used to argue that the change from a flat crack to a slant crack will tend to reduce the level of crack tunneling at a specimen's mid-plane and promote more uniform shearing failure along the crack's slant plane.

4. Summary and conclusions

3D elastic–plastic finite element analyses have been carried out for Arcan 2024-T3 aluminum alloy specimens with flat and slant cracks under remote Mode I loading conditions. The focus of this study has been to compare the stress and deformation fields around flat and slant cracks in order to understand why a flat crack loaded in Mode I tends to grow in a slant manner, with a goal of providing insight for formulating a theory for slant fracture failure often observed in ductile stable tearing tests.

The following observations and conclusions can be drawn from this study:

1. Slant fracture enhances the local tearing COD component, resulting in local mixed-mode I/III conditions along the crack front.
2. The near crack-front crack driving force in terms of the $|\text{COD}|$ is greater in the slant crack case than in the flat crack case.
3. When a flat crack is replaced with a slant crack, the constraint and mean stress at a specimen's mid-plane are reduced while the effective stress both at the specimen's mid-plane and at the front and back surfaces is enhanced.
4. A shearing type of failure is promoted in the case of a slant crack as compared to a tensile type of failure in the case of a flat crack.
5. Crack tunneling is likely less severe in a specimen with a slant crack than in one with a flat crack.

Relative to the first item above, it is worth noting the results [12] of a preliminary, 3D finite element simulation of the stable tearing crack growth event in the Al 2024-T3 Arcan specimen. In this work, an initially flat flaw is extended in a flat-to-slant manner (see Fig. 1 for the FE mesh) assuming (a) a straight crack front throughout the stable tearing process, (b) a critical COD value of 0.52 mm at 0.50 mm behind the straight crack front (which is consistent with experimental surface measurements [17,18]) and (c) crack extension of the through-thickness crack front when the surface COD achieved the critical value. The predicted variations of δ_i (i.e., $|\text{COD}|$) and its components during this crack growth process are shown in Fig. 17. An important observation from this figure is that, at the early stage of crack growth when the crack surface is still flat, the shearing (local Mode II) and tearing (local Mode III) COD components, δ_{II} and δ_{III} , are basically zero, indicating an opening (local Mode I) type crack growth. When the crack turns and grows along the slant crack surface, however, δ_{I} and δ_{III} are seen to approach each other while δ_{II} remains zero, thus suggesting a combined local mode I/III crack growth.

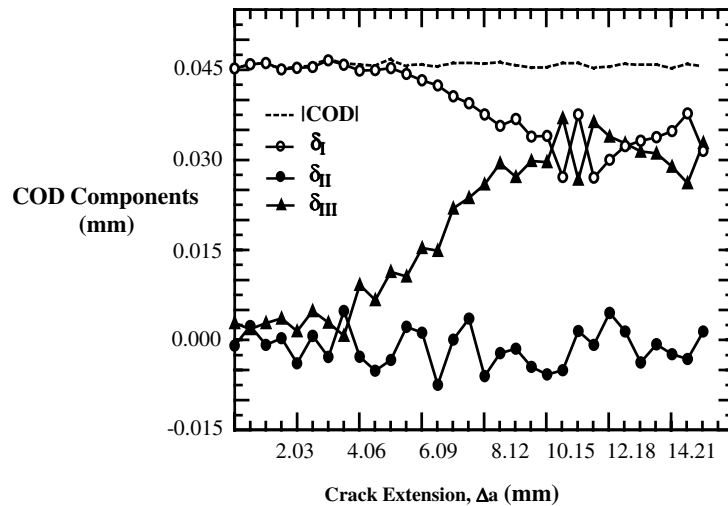


Fig. 17. Predicted COD component variations during the transition of flat to slant crack growth in an Al 2024-T3 Arcan specimen under remote Mode I loading conditions, where δ_I , δ_{II} , and δ_{III} are, respectively, the opening, shearing, and tearing components (from [12]).

Acknowledgements

This work was supported in part by AFRL (contract no. 00-3210-27-1), NASA/EPSCoR (grant no. NCC5-174) and the SC Space Grant Consortium. The support of Major Scott Fawaz at the US Air Force Academy and Dr. Julius Dasch at NASA Headquarters is gratefully acknowledged.

References

- [1] Gao X, Shih CF. A parametric study of mixed-mode I/III ductile fracture in tough materials under small scale yielding. *Engng Fract Mech* 1998;60:407–20.
- [2] Kumar AM, Hirth JP. Mixed-mode I/III fracture testing. *Scripta Metall Mater* 1991;25:985–90.
- [3] Jones RH, Li H, Hirth JP. Effects of mixed-mode I/III loading on environment-induced cracking. *Engng Fract Mech* 2001;68:789–801.
- [4] Raghavachary S, Rosenfield AR, Hirth JP. Mixed-mode I/III fracture toughness of an experimental rotor steel. *Metall Trans A* 1990;21A:2539–45.
- [5] Kamat SV, Hirth JP. Mixed mode fracture toughness of engineering materials. *J Engng Mater Technol* 1995;117:391–4.
- [6] Miglin MT, Hirth JP, Rosenfield AR. Development of fractograph features during shear failure of an HSLA steel. *Res Mech* 1984;11:85–95.
- [7] Schroth JG, Hirth JP, Hoagland RG, Rosenfield AR. Combined Mode I–Mode III fracture of a high strength low-alloy steel. *Metall Trans A* 1987;18A:1061–72.
- [8] Miglin MT, Lin IH, Hirth JP, Rosenfield AR. Mixed-mode crack growth using the compact specimen. *ASTM STP 791 Fract Mech* 1983;353–369.
- [9] Kamat SV, Hirth JP. A mixed mode I/III fracture toughness correlation. *Scripta Metall Mater* 1994;30:145–8.
- [10] Li H, Jones RH, Hirth JP. Mixed mode I/III fracture toughness of a V–5Cr–5Ti Alloy at 100 °C. *Scripta Metall Mater* 1995;32:611–6.
- [11] Kamat SV, Srinivas M, Rama Rao P. Mixed mode I/III fracture toughness of Armco Iron. *Acta Metall* 1998;46:4985–92.
- [12] Deng X, Sutton MA, Zuo J, Wang L. Mixed-mode fracture analysis of airframe materials. Proceedings of the fifth Joint NASA/FAA/DoD Conference on Aging Aircraft, Kissimmee, FL, 10–13 September 2001.
- [13] Dawicke DS, Sutton MA. CTOA and crack tunneling measurements in thin sheet 2024-T3 aluminum alloy. *Experiment Mech* 1994;34:357–68.

- [14] Dawicke DS, Sutton MA. Crack tip opening angle measurements and crack tunneling under stable tearing in thin sheet 2024-T3 aluminum alloy. NASA Contractor Report 191523, Hampton, Virginia, September 1993.
- [15] Manoharan M. Development of a mixed-mode fracture mechanism map and its extension to mixed-mode impact Fracture. Recent advances in fracture, proceedings of a symposium held at the Annual Meeting of the Minerals, Metals and Materials Society 1997:373–384.
- [16] Randolph LW, Piascik RS. Three-dimensional crack growth assessment by microtopographic examination. ASTM STP 1256 on Fracture Mechanics 95:303–318.
- [17] Amstutz BE, Sutton MA, Dawicke DS, Newman Jr., JC. An experimental study of COD for mode I/II stable crack growth in thin 2024-T3 aluminum specimens. ASTM STP 1256 on Fract Mech 1995:256–271.
- [18] Boone ML. Characterization of stable tearing in thin sheet 2024-T3 aluminum alloy under tension-torsion loading conditions. Master's thesis, Department of Mechanical Engineering, University of South Carolina, 1999.
- [19] ANSYS Finite Element Code, ANSYS, Inc. Canonsburg, PA.
- [20] Arcan M, Hashin Z, Voloshin A. A method to produce uniform plane stress state with applications to fiber-reinforced materials. Experiment Mech 1978;18:141–6.
- [21] Sutton MA, Deng X, Ma F, Newman Jr JC, James M. Development and application of a crack tip displacement-based mixed mode fracture criterion. Int J Solids Struct 2000;37:3591–618.
- [22] Deng X, Newman Jr JC. A study of some issues in stable tearing crack growth simulations. Engng Fract Mech 1999;64:291–304.
- [23] Ma F, Deng X, Sutton MA, Newman JC Jr., A CTOD-based mixed mode fracture criterion. ASTM STP 1359 on Mixed Mode Crack Behavior 1999:86–110.
- [24] Sutton MA, Helm JD, Boone ML. Experimental study of crack growth in thin sheet material under tension–torsion loading. Int J Fract 2001;109:285–301.